The PICTURE-C exoplanetary imaging balloon mission: second flight results and the transition to a new mission, PICTURE-D

Christopher B. Mendillo[a], Kuravi Hewawasam[a], Jason Martel[a], Thaddeus Potter[a], Sunip Mukherjee[a], Timothy A. Cook[a], Supriya Chakrabarti[a], Frans Snik[b], David S. Doelman[b,f], Dan Sirbu[c], Ruslan Belikov[c], Eduardo Bendek[d], Karl Stapelfeldt[d], and Schuyler Grace Wolff[e]

[a]Lowell Center for Space Science and Technology, University of Massachusetts Lowell, 600 Suffolk Street Suite 315, Lowell, MA 01854, USA
[b]Leiden Observatory, Leiden University, P.O. Box 9513, 2300 RA, Leiden, The Netherlands
[c]NASA Ames Research Center, Moffett Field, Mountain View, CA
[d]Jet Propulsion Laboratory, California Institute of Technology, 4800 Oak Grove Drive, Pasadena, CA 91109, USA
[e]Steward Observatory, Department of Astronomy, University of Arizona, 933 N. Cherry Avenue, Tucson, AZ 85721, USA
[f]SRON Netherlands Institute for Space Research, Niels Bohrweg 4, 2333 CA, Leiden, The Netherlands

ABSTRACT

The PICTURE-C balloon mission launched on its second flight from Fort Sumner, NM on September 28, 2022. During this flight, PICTURE-C, which consists of a 60 cm off-axis telescope feeding a vector vortex coronagraph, demonstrated the first high-contrast dark hole from an observatory in a near-space environment. The coronagraph achieved a modest broadband (20%) contrast ratio of 5×10^{-6}, with performance limited by dynamic pointing transients. The low-order wavefront control system achieved optical pointing stabilization of 1 milliarcseconds RMS for intervals of up to 30 seconds between these transients. This paper will summarize the second flight results and present the development path for PICTURE-D, the next generation direct imaging balloon mission.

Keywords: exoplanets, balloon, wavefront control, direct imaging, fine pointing, high-contrast imaging

1. INTRODUCTION

The Planetary Imaging Concept Testbed Using a Recoverable Experiment - Coronagraph (PICTURE-C) mission is a balloon-borne experiment designed to directly image debris-disks and exozodiacal dust around nearby stars in reflected visible light (540-660 nm).[1–5] A primary goal of the mission is to mature key technologies required to directly image exoplanets from space. The mission was designed and built at the UMass Lowell Center for Space Science and Technology (LoCSST). To achieve the high levels of starlight suppression (contrast) necessary to detect faint exoplanetary signals, PICTURE-C uses a vector vortex coronagraph (VVC) coupled with a 60 cm diameter off-axis telescope. The contrast ratio is increased further by employing adaptive optics (deformable mirrors driven by several wavefront sensors) to both stabilize the stellar wavefront at high speed and perform high-precision focal plane wavefront correction using the electric field conjugation (EFC) technique[6,7] to create a zone of enhanced contrast around the star, a so-called "dark hole".

PICTURE-C performed its first flight on September 28, 2019[2] and validated many of the technologies and sub-systems required to meet the science goals of the mission. These included: thermal monitoring and control using over 80 temperature sensors and 16 heaters, on-sky target acquisition using the Wallops Arc Second Pointer

---

Further author information: (Send correspondence to C.B.M.)
C.B.M.: E-mail: christopher_mendillo@uml.edu

Techniques and Instrumentation for Detection of Exoplanets XI, edited by
Garreth J. Ruane, Proc. of SPIE Vol. 12680, 126800F · © 2023 SPIE
0277-786X · doi: 10.1117/12.2677518

(WASP)[8] pointing system, automatic telescope alignment using a hexapod-actuated secondary mirror, and high-speed low-order wavefront control (LOWFC). A charge 4 VVC and a 5-band spectral imaging camera were also demonstrated during the 2019 flight. These were replaced by a charge 6 VVC and a single wide-band imaging system (540-660 nm) for the second flight.[2] The charge 6 VVC is more tolerant to low-order aberrations[9] and the simplified imaging system reduces scattered light and produces higher signal-to-noise ratio (SNR) images.

The second flight of PICTURE-C was attempted first in 2021 from Fort Sumner, but three straight weeks of inclement weather (strong surface and upper-level winds) prevented the mission from launching. The payload was returned to UMass Lowell for eight months of continued development[1] and returned to Fort Sumner in August, 2022. The mission was successfully launched on September 28, 2022 – three years to the day after the first flight. The flight profile was very similar to that of the first flight. The balloon was launched at 8 AM and terminated at 2 AM the following morning – earlier than desired, but required due to its proximity to White Sands Missile Range. The balloon reached a float altitude of 41.8 km, with an ambient air temperature and pressure of -40°C and 2-3 Torr. The payload was successfully recovered with no damage after descending on a parachute and landing 130 miles from the launch facility.

During its second flight, PICTURE-C demonstrated the first coronagraphic dark hole in a near-space environment and $\sim$1 mas pointing stability. The coronagraph achieved an in-flight broadband (20%) contrast of 5×10^{-6} averaged over the 2.5-10 λ/D dark hole. Full details of the flight were published recently[10] and will not be reproduced here. The following sections will discuss post-flight laboratory testing of the PICTURE-C coronagraph and the transition to the next mission, Planetary Imaging Coronagraph Testbed Using a Recoverable Experiment for Debris Disks (PICTURE-D). PICTURE-D aims to characterize disk morphology, constrain dust grain properties, examine planet-dust interactions and calibrate dust models for future exoplanet imaging missions. We present an overview of the PICTURE-D science mission and a number of the system upgrades being integrated for the next two flights, which are scheduled for 2025 and 2027.

2. PICTURE-C POST-FLIGHT TESTING

In the year following the second PICTURE-C flight, while the new PICTURE-D upgrades are being procured, the PICTURE-C coronagraph has been undergoing further laboratory testing and wavefront control development. The goal of this testing has been to reach a raw contrast level of 1×10^{-8} in broadband light. As of yet, we have not reached this target. The following sections detail our progress in this effort.

2.1 dOTF Phase Flattening

The ideal starting point for the EFC algorithm is a wavefront with zero phase aberration at the plane of the coronagraph mask. In practice it is impossible to measure the wavefront at this location using standard interferometric methods without introducing non-common path errors. Phase retrieval methods have long been employed to solve the problem of measuring and correcting the wavefront using an imaging detector in a focal plane.[11–15] Previously, we demonstrated a phase retrieval and correction technique that used multidimensional non-linear optimization to control the coronagraph's low-order deformable mirror (LODM) to correct the point spread function (PSF) at the VVC focus.[1] This was done by replacing the VVC mask with an imaging detector and measuring the PSF directly at the location where the correction was required. We have now adopted a new method that employs the differential optical transfer function (dOTF)[16–18] wavefront sensing technique with a similar experimental setup; a camera is substituted for the VVC mask and commands are sent to the high-order deformable mirror (HODM) to both modulate and correct the PSF. The HODM is a Boston Micromachines Corporation (BMC)[19] 952-actuator Kilo DM. The process is illustrated in Figure 1. To create the wavefront perturbation required for this technique, six actuators along the perimeter of the HODM are pistoned by 50% of their full stroke. The OTF of the poked and unpoked states is calculated by taking the Fourier transform of the PSF image. These are then subtracted to form the dOTF map. The dOTF map shows two pupil phase maps that overlap at the location of the wavefront perturbation. To measure the full pupil, two dOTF maps are made by modulating opposite sides of the pupil. The two phase maps are then stitched together to fill in the overlap region. The full pupil phase map is then inverted and mapped onto the HODM as a correction step with 10% gain. The process iterates until the phase errors reach their noise limit and the PSF stops improving. The correction shown in Figure 1 contains a large focus component due to a slight error in the focal position of

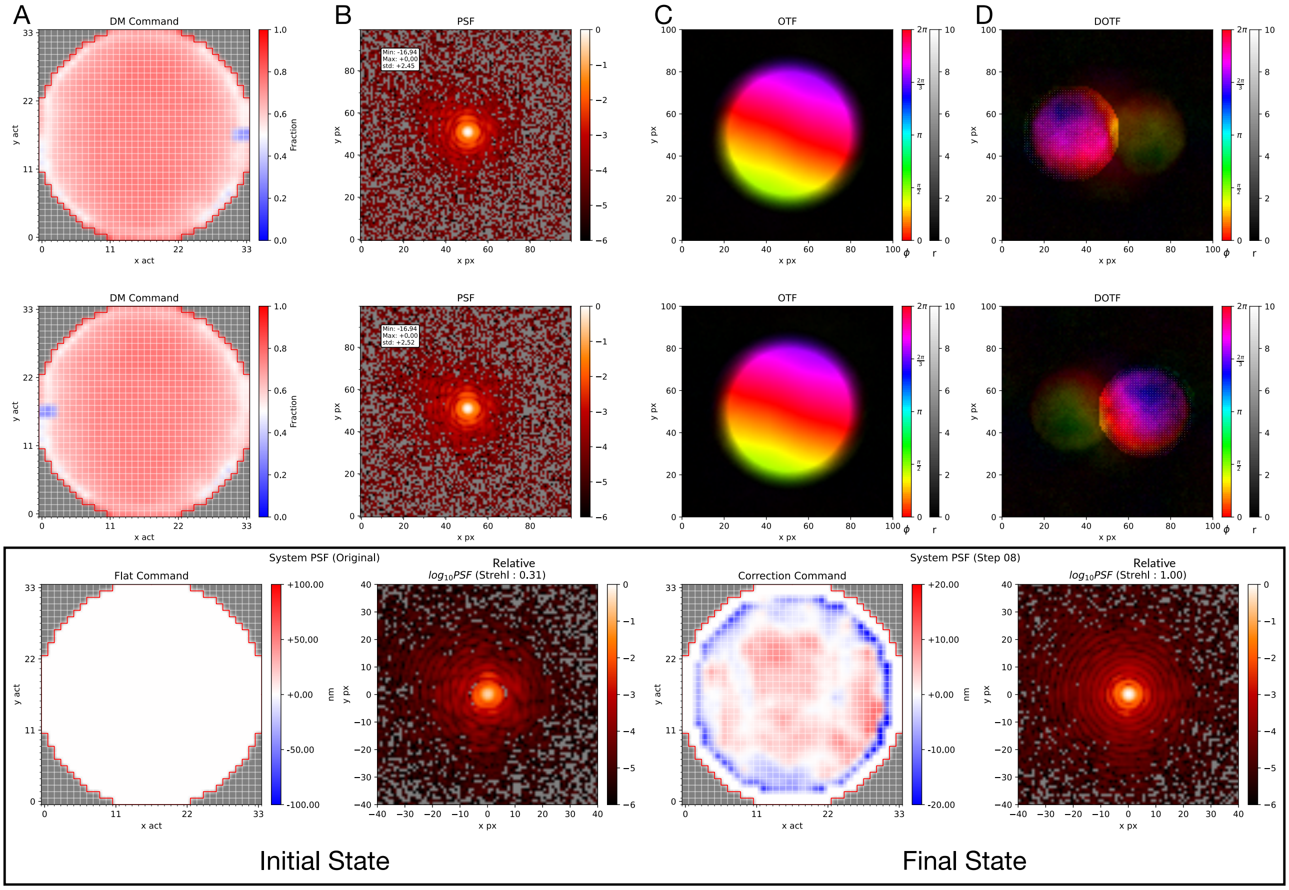

Figure 1. dOTF phase flattening technique applied to the PICTURE-C coronagraph. **A:** HODM command showing perturbation made to six actuators along the right edge of the pupil. **B:** Measured PSF at the VVC focal plane. **C:** Calculated OTF. **D:** dOTF, calculated as the difference between the poked and unpoked OTFs. The same is shown in the second row for the perturbation on the left side of the pupil. The bottom row shows the initial and final state after mapping the dOTF correction on to the HODM.

the camera. In the future this will be corrected by manually shifting the camera position until the focus error is eliminated. The dOTF process was able to improve the relative Strehl ratio by a factor of 3.3.

2.2 Laser Dark Hole

The best broadband (540-660 nm) contrast ratio achieved with the PICTURE-C coronagraph in the lab was 3×10^{-7} averaged over the D-shaped 2.5-10 λ/D dark hole.[1] The system is designed to reach 1×10^{-7} in flight and should be capable of reaching 1×10^{-8} in the lab – without the telescope optics or environmental effects. As a debugging measure, we have been testing the coronagraph with laser light at 633 nm to eliminate all chromatic effects that could be limiting the contrast. In laser light, the contrast improved only to 2×10^{-7}, as shown in the top row of Figure 2. The next step was to eliminate two potential sources of background signal, scattered light from optics downstream of the Lyot stop and charge bleed within the CCD electronics. It is important to remember that all of the light seen outside the dark hole in Figure 2 made it past the Lyot stop. The VVC rejects on-axis starlight only at the 1×10^{-4} level. Wavefront control is responsible for digging the dark hole in that background. This creates the configuration where the edge of the dark hole is a sharp boundary between two illumination patterns that have a 4-5 order of magnitude difference in brightness. This creates the potential for light to scatter back into the dark hole on optics between the Lyot stop and the science camera, and also on the optical structures that comprise the detector itself. In this case, we are using an interline CCD with

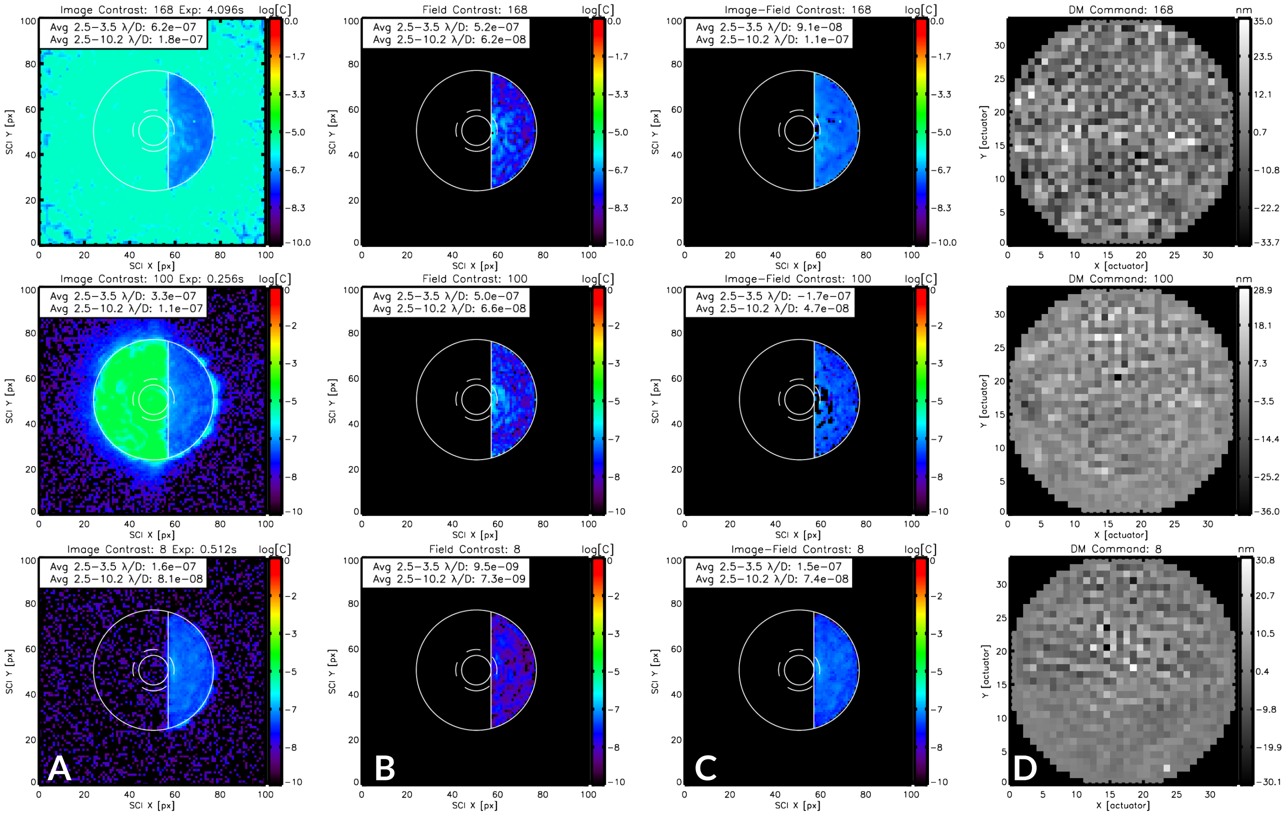

Figure 2. PICTURE-C laboratory dark hole for no field stop (top row), a circular field stop (middle row) and a D-shaped field stop (bottom row). **A:** Raw image contrast. **B:** Field contrast, which is calculated from the electric field estimate used during EFC. **C:** Difference between the image and field contrast. This is an estimate of the incoherent background – the light that is not modulated by the DM during field estimation. **D:** The DM command during this image (relative to the starting flat pattern).

a lenslet array bonded to the front face of the detector to direct light into the active part of each pixel. It is unknown how much light could be scattering within that interface. The charge transfer efficiency of the CCD could also be depositing signal into the dark hole pixels during the readout process – as signal from bright pixels is being clocked through the dark hole region. To mitigate both of these issues, a field stop has been integrated into the instrument after the Lyot stop. The results for a circular and D-shaped stop are shown in the bottom two rows of Figure 2. The contrast ratio showed only marginal improvement to 1×10^{-7} for the circular stop and 8×10^{-8} for the D-shaped stop. For the D-shaped stop, we see the field contrast is 7.3×10^{-9}, which leaves an incoherent background of 7.4×10^{-8}. There are still a number of possible causes for this background. These measurements were made using a single-mode photonic crystal fiber (PCF) as the starting point source. We note that recent tests at the High-Contrast Imaging Testbed (HCIT)[20] use a pinhole spatial filter to avoid background illumination from light leaking into the fiber cladding at the point of injection. It was hoped this would be reduced by switching to the PCF from a traditional stepped-index fiber, but leakage from the fiber source has not been fully ruled out. At this point, we do not believe the DM driver electronics are limiting the performance. PICTURE-C uses a miniature DM driver that was recently tested at the HCIT.[21] Our driver does not have the low-pass filters that were added as a result of that testing to improve in-vacuum performance. Our tests are conducted in air where the driver limit should be 1×10^{-8}.

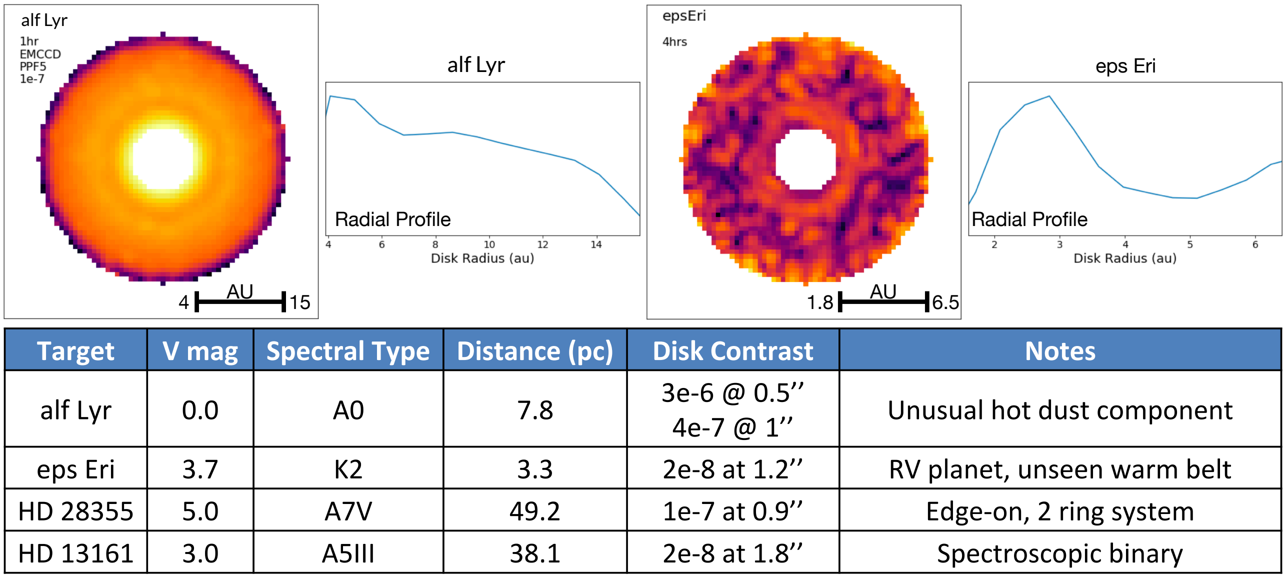

Target	V mag	Spectral Type	Distance (pc)	Disk Contrast	Notes
alf Lyr	0.0	A0	7.8	3e-6 @ 0.5” 4e-7 @ 1”	Unusual hot dust component
eps Eri	3.7	K2	3.3	2e-8 at 1.2”	RV planet, unseen warm belt
HD 28355	5.0	A7V	49.2	1e-7 at 0.9”	Edge-on, 2 ring system
HD 13161	3.0	A5III	38.1	2e-8 at 1.8”	Spectroscopic binary

Figure 3. Simulations for the two primary debris disk targets in our sample as seen with PICTURE-D. Disk orientations are adopted from Herschel far-IR images and the radial locations and total intensities are inferred from the infrared SED and an assumed albedo. The radial extent $\Delta R/R$ of the material is hypothetical pending the observations. In all cases, we assume a contrast floor of 1×10^{-7}, a post-processing gain factor of 5 and the low photon noise provided by the EMCCD. The predicted dust rings are detected in one hour for alf Lyr (Vega) and four hours for eps Eri, both achievable in a single-night balloon flight. Four hours per flight are allocated for PSF calibration to enable speckle reduction in post-processing.

3. PICTURE-D SCIENCE MISSION

PICTURE-D is designed to image debris disks, the clouds of dust particles orbiting main-sequence stars that originate from the collisions and sublimation of remnant planetesimals (asteroids, comets, and Kuiper Belt objects). Debris disks are found as far-infrared excess emission around ∼20% of nearby stars by the IRAS, Spitzer, Herschel, or WISE missions.[22] The brightest examples have been directly imaged in scattered light by ground-based instruments such as Spectro-Polarimetric High-contrast Exoplanet REsearch instrument (SPHERE) and Gemini Planet Imager (GPI) and from space using Hubble Space Telescope (HST).

As the primary science goal, PICTURE-D will provide detailed mapping of debris disk morphology in scattered light for several nearby stars. Asymmetries in debris disks have often been explained through shaping by unseen planets: eccentric rings or stellarocentric offsets (e.g. Fomalhaut[23]), needles or swept back wings (e.g. HD 61005[24]), and multiple narrow belts confined by planet induced resonances (e.g. eps Eri[25]) are all signatures of planet formation processes. Optical scattered light is sensitive to the smallest particles in these systems tracing the collisional histories, and is a valuable component in the interpretation of these asymmetries.

As a secondary goal, PICTURE-D will measure the degree of polarization as a function of scattering angle to break degeneracies in dust properties (e.g. size, porosity, and composition). Dust properties are notoriously degenerate and require assumptions about the dust density distribution. Most debris disks (and indeed solar system objects) all share a distinct scattering phase function (SPF) shape, strong forward and back scattering peaks with a shallow intermediate slope, implying that this is a poor diagnostic for dust composition.[22] However, the degree of polarization and its changes with scattering angle is highly sensitive to both composition and porosity.[26] We aim to extract the total intensity and polarized SPFs for the disk targets described below and use them to constrain dust grain models.

The PICTURE-D targets (Figure 3) are selected from a master list of Spitzer, Herschel, and WISE debris disks within 50 pc. The observed infrared excesses allow a characteristic dust temperature to be derived for each. The dust temperature can be used to infer an approximate orbital distance for the dust, assuming values of the minimum grain size derived from the results of modeling resolved debris disks.[27,28] The sources where dust is

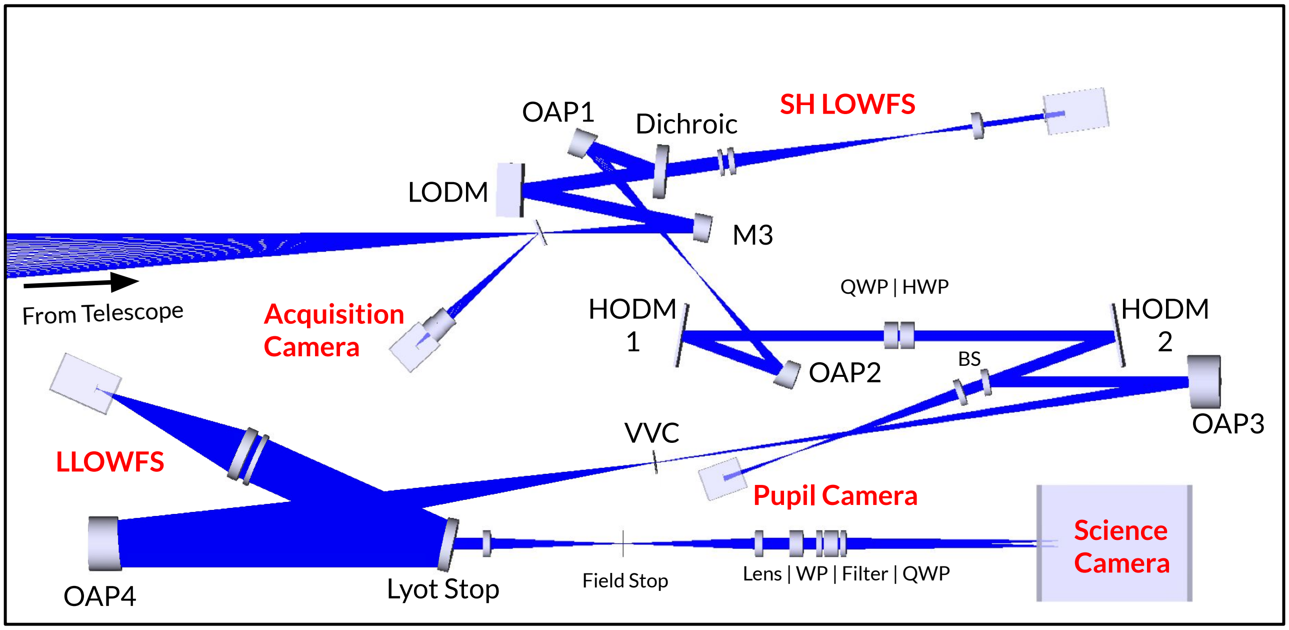

Figure 4. The PICTURE-D coronagraph contains two high-order deformable mirrors (HODM), a low-order wavefront control system fed by two wavefront sensors (SH LOWFS and LLOWFS), a polarimetry mode and a photon-counting science camera. Imaging sensors are shown in red.

inferred to lie inside the PICTURE-D field of view (FOV) (0.5″-2.1″), and for which the disk's fractional infrared luminosity will result in detectable (SNR > 5) surface brightnesses in scattered light, were selected. The final target list is those that are accessible from Ft. Sumner, NM in September, and which have V < 5.0 for adequate wavefront stabilization. All have been previously resolved at low resolution by Herschel in the far-infrared, but none have been detected to date in scattered light. PICTURE-D can expect only a single night of observing for each flight from Fort Sumner. Therefore a realistic observing strategy is to concentrate on one science target per flight. The two primary targets, alf Lyr and eps Eri (Figure 3), are chosen for their predicted brightness and scientific impact.

4. PICTURE-D OPTICAL DESIGN AND UPGRADES

PICTURE-D will fly the same 60 cm off-axis telescope as PICTURE-C.[10] The updated optical design for the PICTURE-D coronagraph is shown in Figure 4. The layout is very similar to PICTURE-C and will reuse the same 48×24 inch carbon fiber optical bench. The notable upgrades are detailed in the following sections.

4.1 Second DM

The new design includes two HODMs to enable a circularly symmetric dark hole around the star – instead of the one-sided D-shaped dark hole from PICTURE-C. The HODMs will be 952-actuator Kilo DMs manufactured by BMC[19] and controlled by a new 20-bit controller (which is currently undergoing testing in the HCIT at JPL).

4.2 Photon-Counting Science Camera

It has long been recognized that photon counting detectors have the power to greatly improve direct imaging science.[29–34] Coronagraphs work in the photon-starved regime and the readout noise of typical CCD electronics can greatly increase the required exposure time to measure an exoplanetary signal at high significance. PICTURE-C flew a traditional CCD detector with 3 e- root mean square (RMS) read noise. To extract the highest scientific gain from the limited observation time of a single-night balloon flight, PICTURE-D will upgrade the science detector to a photon counting detector. We are currently conducting a trade study between two possible flight detectors: the HNü-1024 electron multiplying CCD (EMCCD) from NüVü[35] and the Orca Quest quantitative

NuVu H-Nu EMCCD

- 13 micron pixels
- 1024 x 1024 resolution
- EM Gain up to 5000x
- Single photon counting
- 800,000 e- full well
- COTS version of Roman Detectors
- QE 90% @ 600nm
- Custom passive cooling from HiCIBaS

Hamamatsu Orca Quest qCMOS

- 4.6 micron pixels
- 4096 x 2304 resolution
- Ultra low 0.27 e- read noise
- Photon number resolving (up to 200 per frame)
- 7000 e- full well
- Drop-in replacement for PICTURE-C camera
- QE 80% @ 600nm
- Passive cooling by PICTURE team

Figure 5. The HNü-1024 EMCCD from NüVü[35] and the Orca Quest qCMOS detector from Hamamatsu[36] are being considered for the PICTURE-D flight science detector.

CMOS (qCMOS) detector from Hamamatsu.[36] Versions of the EMCCD have flown on the High-Contrast Imaging Balloon System (HiCIBaS)[29,34] and Faint Intergalactic-medium Redshifted Emission Balloon (FIREBall)[37] balloon missions. The detector is a commercial off-the-shelf (COTS) version of the one selected for the Nancy Grace Roman Space Telescope (Roman) Coronagraph.[32] The qCMOS detector is much newer and has no flight heritage yet. Details of the two cameras are given in Figure 5.

4.3 dgVVC + Polarimetry

The scattered light signal from debris disks can be highly polarized due to the single scattering geometry. PICTURE-D will develop and fly a new, high-throughput polarimetric imaging system that will maximize the science return of the mission. The goal of this system is to measure both orthogonal polarization states simultaneously at high contrast, something that has not previously been possible due to limitations in both the VVC fabrication and the wavefront control algorithm. The PICTURE-D polarimetry approach is enabled by integrating two new technologies: the dgVVC[38] and dual-polarization EFC.[39]

The traditional VVC phase plate that flew on PICTURE-C is limited to operating in one circular polarization at a time. Non-uniformities of the spiral phase retardance pattern that arise during the liquid crystal fabrication process cause stellar leakage at the level of 1×10^{-4}. The typical solution is to employ polarization leakage filtering,[40] which removes this leakage by placing the VVC between crossed circular polarizers. A necessary disadvantage of this system is that it only transmits one polarization state to the science camera. The dgVVC uses the same liquid crystal technology to implement a VVC in a different way, using stacked diffraction gratings, which allows the leakage to be filtered without removing one polarization.

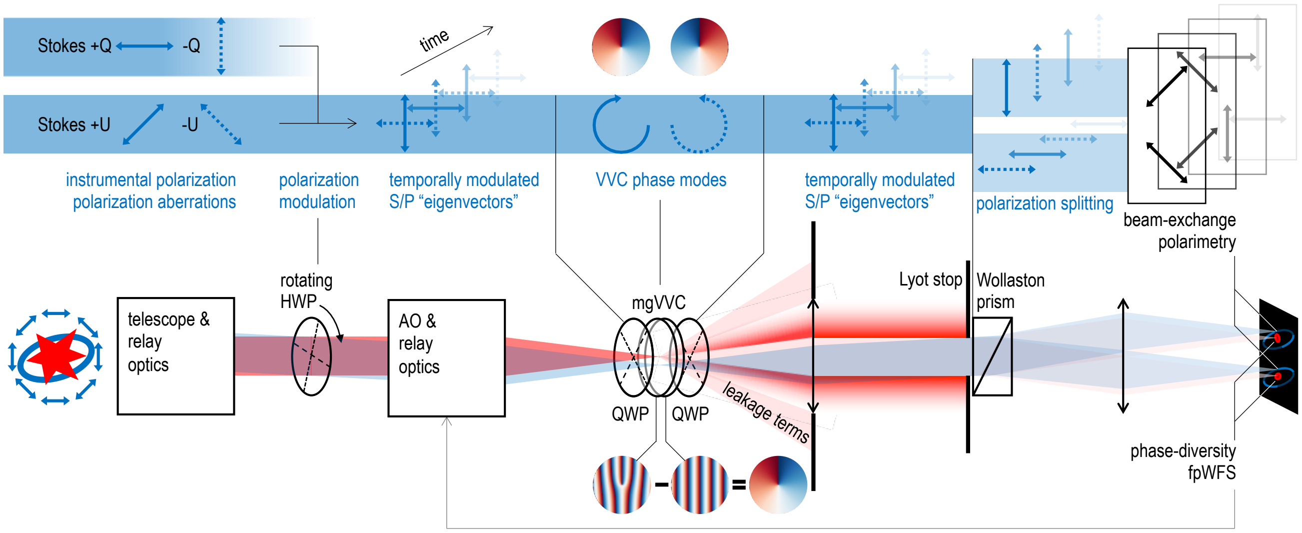

Figure 6. Polarimetry concept schematic for PICTURE-D. A pair of quarter wave plates (QWPs) (center) transform linear polarization on the sky into circular polarization at the dgVVC and back to linear polarization at the detector. The rotating half wave plate (HWP) modulates the polarization at four different angles to reconstruct the full linear Stokes U & Q polarization vectors, thus a set of 4 exposures will be required to make a full polarization measurement.

The second half of the problem is to devise a wavefront control system that can produce a high-contrast dark zone in the presence of wavefront aberrations for both polarizations simultaneously. To accomplish this, we have extended the broadband EFC technique[6] to dual-polarization EFC.[39] In the optical system, a Wollaston prism is used to create two side-by-side images of the sky in orthogonal linear polarizations (Figure 4). Dual-polarization EFC solves the linearized system of equations for a set of DM commands optimized to create a dark zone in both images (polarizations) at the same time. A traditional polarimetric imaging system (Figure 6) will be constructed around these two new technologies by implementing a rotating HWP modulator upstream of the dgVVC. A pair of QWPs are integrated into the dgVVC to create the correct polarization mapping from the science camera to the sky.[41] An added benefit of the dual-polarization camera is that the phase diversity between the two images can be used to directly reconstruct the electric field[42,43] without implementing focal plane wavefront sensing (FPWFS)[6,44] probe patterns on the DM. This provides a factor of four increase in the dark zone convergence speed because one image is used to measure the field instead of four. It also removes the cross-coupling between the FPWFS and reflective Lyot-stop LOWFS (LLOWFS).[45]

4.3.1 Multi-Star Wavefront Control

MSWC[46–48] is a method that enables existing (single-star) coronagraphs, such as the one on PICTURE-D, to image exoplanets and disks around binary star systems. MSWC is primarily a wavefront control algorithm that works with existing coronagraphs and wavefront control systems. It uses one set of deformable mirror modes (for example, low spatial frequencies) to suppress speckles from the on-axis coronagraphically blocked star and another set (for example, high spatial frequencies) to suppress speckles from the off-axis star. Because the off-axis star is typically well separated, a second coronagraph is not required, but wavefront control is. If the desired dark zone is beyond the Nyquist limit of the DM with respect to the off-axis star, the DM is operated in a super-Nyquist mode, which is achieved by having a mild grating in the system. Such a grating is already present on PICTURE-D as a side effect of BMC DM manufacture (so-called "DM quilting").

PICTURE-D will conduct an on-sky demonstration of MSWC. Simulations of MSWC for PICTURE-D are shown in Figure 7 for bet Gem A (Castor) and its binary companion. This is the primary target because its super-Nyquist separation make it an analogue to the alpha Cen binary system, the most sought after binary target,[33] which is only visible in the southern hemisphere and will be observed by the Roman Coronagraph.

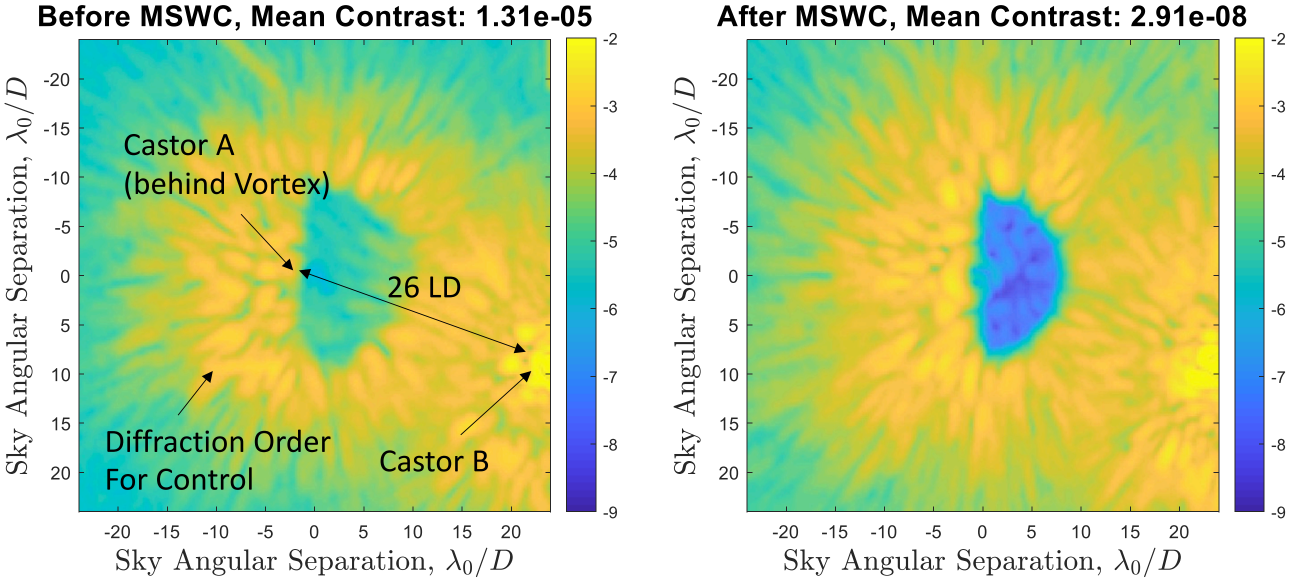

Figure 7. Simulations of PICTURE-D MSWC on bet Gem A (Castor). Without MSWC, the contrast would be limited to 1.3×10^{-5} (left). Using MSWC, the contrast can be improved to 2.9×10^{-8} over the PICTURE-D 20% bandpass.

4.4 Other Upgrades

To improve the raw starlight rejection of the VVC, the F-number of the VVC beam has been increased from 24.3 to 56.8. This enlarges the stellar spot on the mask, reducing the leakage caused by irregularities near the central singularity of the vortex pattern. The system also includes a new pupil imaging camera that will allow us to check the HODM centering on the telescope beam. Related to the DM centering, the new optical design produces a slightly oversized pupil image at the first HODM, which contains an aperture mask that will reduce the beam down to the 9 mm diameter required to fit on the BMC DM. With PICTURE-C, the pupil was defined by the primary mirror edge and we attempted to reimage this directly to the DM while maintaining < 50 micron pupil centering. Since there is no absolute fiducial for the telescope boresight, it is possible to end up in a configuration where the telescope is being used slightly off-axis with the induced wavefront error corrected by the secondary mirror and LODM. This has the potential to shift the pupil location on the HODM, which could invalidate the EFC matrix used to create the dark hole. We chose to sacrifice 12% of the telescope diameter to ensure the pupil is always centered on the HODM. In addition to the science camera upgrade, all of the wavefront sensor cameras and the acquisition camera will be upgraded to adopt the Sony IMX421 CMOS sensor, which offers higher frame rates and quantum efficiency than the detectors flown on PICTURE-C. The mission will also fly a completely new flight computer stack built on the PCIe-104 standard, which is required to maintain compatibility with the new wavefront sensor cameras. The CPU is a quad-core Intel Xeon processor and the high-speed cameras are run on the CameraLink-Full interface.

5. CONCLUSIONS

During its second flight, PICTURE-C demonstrated the first on-sky use of focal plane wavefront sensing and EFC in a near-space environment.[10] These techniques were used to create a coronagraphic dark hole with a raw contrast of 5×10^{-6} averaged from 2.5-10 λ/D. The mission also demonstrated 1 mas RMS pointing stabilization. Ongoing development and laboratory testing of the PICTURE-C coronagraph has continued in the year following the second flight with the goal of reaching a raw contrast of 1×10^{-8} in the lab. The next round of testing will investigate the single-mode fiber source, VVC mask imperfections and effects from in-air testing as potential sources of incoherent background.

Over the next year we will begin integrating several upgrades for PICTURE-D. The detectors and DMs will be upgraded first with the traditional VVC that flew on PICTURE-C. The dgVVC is undergoing active development at Leiden University[38, 49] and will be integrated along with the polarimetry optics as soon as it is ready. MSWC laboratory testing will begin in 2024 in preparation for the next flight. PICTURE-D is scheduled to fly in the fall of 2025 and 2027.

ACKNOWLEDGMENTS

This work was funded under NASA grants NNX15AG23G, 80NSSC21K1919 and 80NSSC22K1648. The PICTURE team would like to acknowledge and thank Emiel H. Por for his guidance in implementing the dOTF technique.

REFERENCES

[1] C. B. Mendillo, K. Hewawasam, J. Martel, T. Potter, T. A. Cook, and S. Chakrabarti, "The PICTURE-C exoplanetary imaging balloon mission: laboratory coronagraph demonstrations of high-contrast imaging and low-order wavefront control," in *Space Telescopes and Instrumentation 2022: Optical, Infrared, and Millimeter Wave*, L. E. Coyle, S. Matsuura, and M. D. Perrin, eds., **12180**, p. 1218022, International Society for Optics and Photonics, SPIE, 2022.

[2] C. B. Mendillo, K. Hewawasam, J. Martel, T. Potter, T. A. Cook, and S. Chakrabarti, "The picture-c exoplanetary imaging balloon mission: First flight results and second flight preparation," in *Techniques and Instrumentation for Detection of Exoplanets X*, S. B. Shaklan and G. J. Ruane, eds., SPIE, aug 2021.

[3] C. B. Mendillo, G. A. Howe, K. Hewawasam, J. Martel, S. C. Finn, T. A. Cook, and S. Chakrabarti, "Optical tolerances for the picture-c mission: error budget for electric field conjugation, beam walk, surface scatter, and polarization aberration," *Proc.SPIE* **10400**, p. 17, 2017.

[4] C. B. Mendillo, J. Brown, J. Martel, G. A. Howe, K. Hewasawam, S. C. Finn, T. A. Cook, S. Chakrabarti, E. S. Douglas, D. Mawet, O. Guyon, G. Singh, J. Lozi, K. L. Cahoy, and A. D. Marinan, "The low-order wavefront sensor for the picture-c mission," in *Techniques and Instrumentation for Detection of Exoplanets VII*, *Proc. SPIE* **9605**, p. 19, Sept. 2015.

[5] T. Cook, K. Cahoy, S. Chakrabarti, E. Douglas, S. C. Finn, M. Kuchner, N. Lewis, A. Marinan, J. Martel, D. Mawet, B. Mazin, S. R. Meeker, C. Mendillo, G. Serabyn, D. Stuchlik, and M. Swain, "Planetary imaging concept testbed using a recoverable experiment-coronagraph (picture c)," *Journal of Astronomical Telescopes, Instruments, and Systems* **1**, p. 044001, Oct. 2015.

[6] A. Give'on, B. Kern, S. Shaklan, D. C. Moody, and L. Pueyo, "Broadband wavefront correction algorithm for high-contrast imaging systems," *Proc. SPIE* **6691**, Sept. 2007.

[7] A. Give'on, B. D. Kern, and S. Shaklan, "Pair-wise, deformable mirror, image plane-based diversity electric field estimation for high contrast coronagraphy," in *Techniques and Instrumentation for Detection of Exoplanets V*, S. Shaklan, ed., *Society of Photo-Optical Instrumentation Engineers (SPIE) Conference Series* **8151**, p. 815110, Oct. 2011.

[8] D. W. Stuchlik and R. J. Lanzi, "The nasa wallops arc-second pointer (wasp) system for precision pointing of scientific balloon instruments and telescopes," (20180002870).

[9] D. Mawet, L. Pueyo, D. Moody, J. Krist, and E. Serabyn, "The vector vortex coronagraph: sensitivity to central obscuration, low-order aberrations, chromaticism, and polarization," *Proc. SPIE* **7739**, p. 14, July 2010.

[10] C. B. Mendillo, K. Hewawasam, J. Martel, T. Potter, T. A. Cook, and S. Chakrabarti, "Balloon flight demonstration of coronagraph focal plane wavefront correction with PICTURE-C," **9**(02).

[11] J. R. Fienup, "Reconstruction of an object from the modulus of its fourier transform," **3**(1), p. 27.

[12] J. E. Krist and C. J. Burrows, "Phase-retrieval analysis of pre-and post-repair hubble space telescope images," *ApOpt* **34**, pp. 4951–4964, Aug. 1995.

[13] P. Riaud, D. Mawet, and A. Magette, "Nijboer-zernike phase retrieval for high contrast imaging. principle, on-sky demonstration with naco, and perspectives in vector vortex coronagraphy," *A&A* **545**, p. A150, Sept. 2012.

[14] D. Marx and B. Kern, "Phase retrieval implementation for the WFIRST coronagraph development testbed," in *Imaging and Applied Optics 2016*, OSA.

[15] G. R. Brady, C. Moriarty, P. Petrone, I. Laginja, K. Brooks, T. Comeau, L. Leboulleux, and R. Soummer, "Phase-retrieval-based wavefront metrology for high contrast coronagraphy," in *Space Telescopes and Instrumentation 2018: Optical, Infrared, and Millimeter Wave*, H. A. MacEwen, M. Lystrup, G. G. Fazio, N. Batalha, E. C. Tong, and N. Siegler, eds., SPIE.

[16] J. L. Codona, "Differential optical transfer function wavefront sensing," **52**(9), p. 097105.

[17] V. Korkiakoski, N. Doelman, J. Codona, M. Kenworthy, G. Otten, and C. U. Keller, "Calibrating a high-resolution wavefront corrector with a static focal-plane camera," **52**(31), p. 7554.

[18] R. Soummer, E. H. Por, R. Pourcelot, S. F. Redmond, I. Laginja, S. D. Will, M. D. Perrin, L. Pueyo, A. Sahoo, P. Petrone, K. J. Brooks, R. Fox, A. Klein, B. Nickson, T. Comeau, M. Ferrari, R. Gontrum, J. Hagopian, L. Leboulleux, D. Leongomez, J. Lugten, L. M. Mugnier, M. N'Diaye, M. Nguyen, J. Noss, J.-F. Sauvage, N. Scott, A. Sivaramakrishnan, H. B. Subedi, and S. Weinstock, "High-contrast imager for complex aperture telescopes (HiCAT): 8. dark zone demonstration with simultaneous closed loop low-order wavefront sensing and control," in *Space Telescopes and Instrumentation 2022: Optical, Infrared, and Millimeter Wave*, L. E. Coyle, M. D. Perrin, and S. Matsuura, eds., SPIE.

[19] www.bostonmicromachines.com. Boston Micromachines website.

[20] G. J. Ruane, A. J. E. Riggs, E. Serabyn, W. Baxter, C. M. Prada, D. Mawet, M. R. Noyes, P. K. Poon, and N. Tabiryan, "Broadband vector vortex coronagraph testing at NASA's high contrast imaging testbed facility," in *Space Telescopes and Instrumentation 2022: Optical, Infrared, and Millimeter Wave*, L. E. Coyle, M. D. Perrin, and S. Matsuura, eds., SPIE.

[21] E. A. Bendek, G. J. Ruane, C. M. Prada, C. B. Mendillo, A. E. Riggs, and E. Serabyn, "Microelectromechanical deformable mirror development for high-contrast imaging, part 1: miniaturized, flight-capable control electronics," *Journal of Astronomical Telescopes, Instruments, and Systems* **6**(4), pp. 1 – 20, 2020.

[22] A. M. Hughes, G. Duchêne, and B. C. Matthews, "Debris disks: Structure, composition, and variability," *Annual Review of Astronomy and Astrophysics* **56**, pp. 541–591, sep 2018.

[23] P. Kalas, J. R. Graham, and M. Clampin, "A planetary system as the origin of structure in Fomalhaut's dust belt," *Nature* **435**, pp. 1067–1070, June 2005.

[24] T. M. Esposito, M. P. Fitzgerald, J. R. Graham, P. Kalas, E. J. Lee, E. Chiang, G. Duchêne, J. Wang, M. A. Millar-Blanchaer, E. Nielsen, S. M. Ammons, S. Bruzzone, R. J. De Rosa, Z. H. Draper, B. Macintosh, F. Marchis, S. A. Metchev, M. Perrin, L. Pueyo, A. Rajan, F. T. Rantakyrö, D. Vega, and S. Wolff, "Bringing "The Moth" to Light: A Planet-sculpting Scenario for the HD 61005 Debris Disk," *AJ* **152**, p. 85, Oct. 2016.

[25] M. Booth, W. R. F. Dent, A. Jordán, J.-F. Lestrade, A. S. Hales, M. C. Wyatt, S. Casassus, S. Ertel, J. S. Greaves, G. M. Kennedy, L. Matrà, J.-C. Augereau, and E. Villard, "The Northern arc of Epsilon Eridani's Debris Ring as seen by ALMA," *Monthly Notices of the Royal Astronomical Society* **469**, pp. 3200–3212, Aug. 2017.

[26] M. D. Perrin, G. Schneider, G. Duchene, C. Pinte, C. A. Grady, J. P. Wisniewski, and D. C. Hines, "The case of ab aurigae's disk in polarized light: Is there truly a gap?," *ApJL* **707**, pp. L132–L136, Dec. 2009.

[27] J. E. Krist, K. R. Stapelfeldt, G. Bryden, G. H. Rieke, K. Y. L. Su, C. H. Chen, C. A. Beichman, D. C. Hines, L. M. Rebull, A. Tanner, D. E. Trilling, M. Clampin, and A. Gáspár, "HST and Spitzer Observations of the HD 207129 Debris Ring," *AJ* **140**, pp. 1051–1061, Oct. 2010.

[28] D. A. Golimowski, J. E. Krist, K. R. Stapelfeldt, C. H. Chen, D. R. Ardila, G. Bryden, M. Clampin, H. C. Ford, G. D. Illingworth, P. Plavchan, G. H. Rieke, and K. Y. L. Su, "HUBBLEANDSPITZER SPACE TELESCOPEOBSERVATIONS OF THE DEBRIS DISK AROUND THE NEARBY k DWARF HD 92945," *The Astronomical Journal* **142**, p. 30, jun 2011.

[29] O. Daigle, O. Djazovski, D. Laurin, R. Doyon, and É. Artigau, "Characterization results of EMCCDs for extreme low-light imaging," in *High Energy, Optical, and Infrared Detectors for Astronomy V*, A. D. Holland and J. W. Beletic, eds., SPIE, sep 2012.

[30] A. N. Wilkins, M. W. McElwain, T. J. Norton, B. J. Rauscher, J. F. Rothe, M. Malatesta, G. M. Hilton, J. R. Bubeck, C. A. Grady, and D. J. Lindler, "Characterization of a photon counting EMCCD for space-based high contrast imaging spectroscopy of extrasolar planets," in *High Energy, Optical, and Infrared Detectors for Astronomy VI*, A. D. Holland and J. Beletic, eds., SPIE, jul 2014.

[31] C. Marois, C. Bradley, J. Pazder, R. Nash, S. Metchev, F. Grandmont, A.-L. Maire, R. Belikov, B. Macintosh, T. Currie, R. Galicher, F. Marchis, D. Mawet, E. Serabyn, and E. Steinbring, "Maple: reflected light from exoplanets with a 50-cm diameter stratospheric balloon telescope," in *Society of Photo-Optical Instrumentation Engineers (SPIE) Conference Series*, *Society of Photo-Optical Instrumentation Engineers (SPIE) Conference Series* **9143**, p. 2, Aug. 2014.

[32] L. K. Harding, R. T. Demers, M. Hoenk, P. Peddada, B. Nemati, M. Cherng, D. Michaels, L. S. Neat, A. Loc, N. Bush, D. Hall, N. Murray, J. Gow, R. Burgon, A. Holland, A. Reinheimer, P. R. Jorden, and D. Jordan, "Technology advancement of the CCD201-20 EMCCD for the WFIRST coronagraph instrument: sensor characterization and radiation damage," *Journal of Astronomical Telescopes, Instruments, and Systems* **2**, p. 011007, dec 2015.

[33] E. A. Bendek, R. Belikov, J. Lozi, S. Thomas, J. Males, S. Weston, and M. McElwain, "Space telescope design to directly image the habitable zone of alpha centauri," in *Techniques and Instrumentation for Detection of Exoplanets VII*, S. Shaklan, ed., SPIE, sep 2015.

[34] O. Côté, G. Allain, D. Brousseau, M.-P. Lord, S. Ouahbi, M. Ouellet, D. Patel, S. Thibault, C. Vallée, C. Bradley, O. Daigle, R. Doyon, M. Helmbrecht, M. A. Kenworthy, D. Lafrenière, F. Marchis, C. Marois, S. Montminy, F. Snik, G. Vasisht, J.-P. Véran, P. Vincent, R. Belikov, E. A. Bendek, F. Grandmont, D. Doelman, C. Blain, and C. de Jong, "A precursor mission to high contrast imaging balloon system," in *Ground-based and Airborne Instrumentation for Astronomy VII*, H. Takami, C. J. Evans, and L. Simard, eds., SPIE, jul 2018.

[35] www.nuvucameras.com. NuVu website.

[36] www.hamamatsu.com. Hamamatsu website.

[37] E. T. Hamden, N. Lingner, G. Kyne, P. Morrissey, and D. C. Martin, "Noise and dark performance for FIREBall-2 EMCCD delta-doped CCD detector," in *UV, X-Ray, and Gamma-Ray Space Instrumentation for Astronomy XIX*, O. H. Siegmund, ed., SPIE, sep 2015.

[38] D. S. Doelman, E. H. Por, G. Ruane, M. J. Escuti, and F. Snik, "Minimizing the polarization leakage of geometric-phase coronagraphs with multiple grating pattern combinations," *Publications of the Astronomical Society of the Pacific* **132**, p. 045002, mar 2020.

[39] C. B. Mendillo, K. Hewawasam, J. Martel, T. A. Cook, S. Chakrabarti, F. Snik, and D. Doelman, "Dual-polarization electric field conjugation and applications for vector vortex coronagraphs," in *Techniques and Instrumentation for Detection of Exoplanets X*, S. B. Shaklan and G. J. Ruane, eds., SPIE, jul 2021.

[40] D. Mawet, E. Serabyn, D. Moody, B. Kern, A. Niessner, A. Kuhnert, D. Shemo, R. Chipman, S. McClain, and J. Trauger, "Recent results of the second generation of vector vortex coronagraphs on the high-contrast imaging testbed at jpl," *Proc. SPIE* **8151**, p. 81511D, Sept. 2011.

[41] F. Snik, G. Otten, M. Kenworthy, D. Mawet, and M. Escuti, "Combining vector-phase coronagraphy with dual-beam polarimetry," in *SPIE Proceedings*, S. K. Ramsay, I. S. McLean, and H. Takami, eds., SPIE.

[42] P. Riaud, D. Mawet, and A. Magette, "Instantaneous phase retrieval with the vector vortex coronagraph. theoretical and optical implementation," *A&A* **545**, p. A151, Sept. 2012.

[43] M. Quesnel, G. O. de Xivry, G. Louppe, and O. Absil, "A deep learning approach for focal-plane wavefront sensing using vortex phase diversity," **668**, p. A36.

[44] A. Give'on, N. J. Kasdin, R. J. Vanderbei, and Y. Avitzour, "On representing and correcting wavefront errors in high-contrast imaging systems," *J. Opt. Soc. Am. A* **23**, pp. 1063–1073, May 2006.

[45] C. B. Mendillo, K. Hewawasam, G. A. Howe, J. Martel, T. A. Cook, and S. Chakrabarti, "Decoupling the image-plane and low-order wavefront sensors for the PICTURE-C coronagraph," in *Techniques and Instrumentation for Detection of Exoplanets IX*, S. B. Shaklan, ed., **11117**, pp. 559 – 565, International Society for Optics and Photonics, SPIE, 2019.

[46] S. Thomas, R. Belikov, and E. Bendek, "Techniques for High-contrast Imaging in Multi-star Systems. i. Super-Nyquist Wavefront Control," *The Astrophysical Journal* **810**, p. 81, sep 2015.

[47] D. Sirbu, S. Thomas, R. Belikov, and E. Bendek, "Techniques for high-contrast imaging in multi-star systems. II. multi-star wavefront control," *The Astrophysical Journal* **849**, p. 142, nov 2017.

[48] R. Belikov, E. A. Pluzhnik, E. A. Bendek, and D. Sirbu, "High-contrast imaging in multi-star systems: progress in technology development and lab results," in *Techniques and Instrumentation for Detection of Exoplanets VIII*, S. Shaklan, ed., SPIE, sep 2017.

[49] D. S. Doelman, M. Ouellet, G. Ruane, M. Escuti, S. Haffert, and F. Snik, "First laboratory tests of a triple-grating vector vortex coronagraph," in *Space Telescopes and Instrumentation 2022: Optical, Infrared, and Millimeter Wave*, L. E. Coyle, S. Matsuura, and M. D. Perrin, eds., **12180**, p. 1218029, International Society for Optics and Photonics, SPIE, 2022.